Topology optimisation of friction under-platform dampers using Moving Morphable Components and the Efficient Global Optimization algorithm

Enora Denimal, Ludovic Renson, Chian Wong, Loic Salles

Structural and Multidisciplinary Optimization manuscript No.
(will be inserted by the editor)

Topology optimisation of friction under-platform dampers using Moving Morphable Components and the Efficient Global Optimization algorithm

Enora Denimal · Ludovic Renson · Chian Wong · Loic Salles

Received: date / Accepted: date

Abstract Underplatform dampers (UPDs) are traditionally used in aircraft engines to reduce the risk of high cycle fatigue. By introducing friction in the system, vibrations at resonance are damped. However, UDPs are also the source of nonlinear behaviours making the analysis and the design of such components complex. The shape of such friction dampers has a substantial impact on the damping performances, topology optimisation is seldomly utilised – particularly for nonlinear structures. In the present work, we present a numerical approach to optimise the topology of friction dampers in order to minimise the vibration amplitude at a resonance peak. The proposed approach is based on the Moving Morphable Components framework to parametrise the damper topology, and the Efficient Global Optimisation algorithm is employed for the optimisation. The results demonstrate the relevance of such an approach for the optimisation of nonlinear vibrations in the presence of friction. New efficient damper geometries are identified in a few iterations of the algorithm, illustrating the efficiency of the approach. Results show that the most efficient geometry divides the vibration amplitude at resonance by 3, corresponds to a lower mass (80%) and a smaller frequency shift compared to the non-optimised case. More generally, the different geometries are analysed and tools for clustering are proposed. Different clusters are identified and compared. Thus, more general conclusions can be obtained. More specifically, the most efficient geometries correspond to geometries that reduce the mass of the damper and increase the length of the contact surface. Physically, it corresponds to a reduction of the initial normal contact pressure, which implies that the contact points enter stick/slip earlier, bringing more damping. The results show how topology optimisation can be employed for nonlinear vibrations to identify efficient layouts for components.

Keywords friction damping · topology optimisation · nonlinear vibrations · kriging · efficient global optimisation · moving morphable components

E. Denimal
Univ. Gustave Eiffel, Inria, COSYS-SII, I4S, Campus Beaulieu, 35042 Rennes, France
E-mail: enora.denimal@inria.fr

L. Renson
Dynamics group, Imperial College London, London, United Kingdom

C. Wong
Rolls-Royce plc, Derby DE2 48J, United Kingdom

L. Salles
Skolkovo Institute of Science and Technology, Moscow, Russia

1 Introduction

Friction is often considered to be at the origin of numerous detrimental effects such as excessive wear of components, surface damage, fatigue failures, noise, and friction-induced instabilities. However, using it as a passive solution to reduce vibrations is nowadays a well-established technology [1,2,3]. It is of particular use in the aerospace industry where friction joints can be introduced to improve dynamic behaviour and structure integrity. In weakly damped structures, such as those found in aeronautics, friction is often one of the most important sources of damping. For example, turbine blades are subjected to high thermal, centrifugal and vibration stresses [4,5] which can lead to high cycle fatigue, and thereby to blades failure [6]. Because of the large operating range and of the high modal density of the bladed disk, resonances cannot be avoided. Dry friction is then introduced to either provide enough damping or shift resonance frequencies away from the most critical resonances [7,8]. In this context, dry friction can be introduced directly through the contact between the different blades (shroud, blade tips) or with the disc (roots). However, one of the most efficient solution remains the use of under-platform dampers (UPDs) [7,8,9,10,11]. They consist of a small metal device located in a groove under the platform of adjacent blades. During operation, the contact with the blades platforms is ensured by the centrifugal loading. When the blades vibrate, the relative motion between the blades and the damper generates friction, and so energy is dissipated. The presence of a friction contact interface is the source of strong non-linearities making the study, analysis and design of such components complex [7,9,12,5].

It is well known that the shape of the damper has a substantial influence on its damping properties. The most classical shapes are the wedge damper geometry, illustrated in Figure 1(a) and the cylindrical damper geometry, illustrated in Figure 1(b). They have largely been studied over the last decades, one can refer to [13,14,15,16, 11,17] for the wedge geometry and to [18,13,19] for the cylindrical geometry. To take advantage of both shapes, a mix of them has been investigated in [20,21,22], and an illustrative geometry can be seen in Figure 1(c). More recently, a conical geometry that avoids the well-known rolling motion has been proposed in [23]. Numerous studies have been dedicated to the impact of dampers geometrical properties on their damping performances. First works were based on large parametric studies to identify the best mechanical or geometrical properties. In [13], wedge and cylindrical damper performances are compared for different normal loads and engine orders using the Harmonic Balance Method (HBM) to solve the equation of motion. In [9] a large parametric study is employed to find the optimal damper mass, also based on an HBM formulation for the nonlinear analysis. In [24], the same strategy is employed to find the best mass and platform angles for a cylindrical damper. In [25], the effect of dimensionless parameters of a flattened cylinder damper is investigated based on geometrical and kinematics analyses. More recently, in [26,27] the effect of the shape of ring damper is investigated by either comparing different geometries or by parametrising the Finite Element Model (FEM) of the ring damper based on HBM or Nonlinear Normal Mode (NNM) simulations, respectively. First optimisation works were carried out in [28], where the mass of a wedge damper is robustly optimised to minimize the maximum vibration amplitude by taking into account uncertainties related to the excitation level, the linear damping and the friction coefficient. The nonlinear analysis is based on the NNM formulation. Finally, in [29], a wedge shape is parametrised with its thickness, length and angle and optimised based on a radial basis functions surrogate model, where the FRF are computed using the HBM. The majority of these studies are based on parametric studies where the scanning on a few key design parameters is performed to identify interesting and advantageous damper features, and only a few of them resort to optimisation algorithms [28,29]. This could be explained by different reasons. First, the objective function might be strongly non-convex and its evaluation is often numerically expensive. Moreover, analytical gradients are not available and it would be too expensive to compute them numerically. It makes the use of traditional gradient-based optimisation methods unsuitable. Second, if one wants to consider real world cases, then large FEM are treated. It represents a large computational time related to the nonlinear analysis, especially when the full FRF is computed. It also requires the nonlinear solver to be robust enough to consider a large variety of cases. Moreover, in all these works, only basic parameters are considered as the mass of the damper or a few geometrical properties as length or thickness. In a context where additive manufacturing is becoming accessible and where the shape of such components has a strong influence on the damping properties,

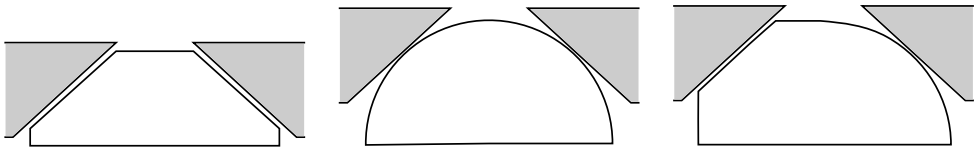

Fig. 1: Sketch of classic UPD shapes: (a) wedge shape, (b) cylindrical shape, (c) mix of wedge and cylindrical shapes

the potential of topology optimisation is obvious. Thus, the objective of the paper is to propose a rigorous and efficient approach to optimise the topology of friction dampers in order to identify new possible shapes with specific features that improve drastically the damping efficiency. Another underlying objective is to investigate how topology optimisation can help in the design, but also in the analysis, of friction dampers. Moreover, the approach tends to be general enough to deal with topology optimisation in nonlinear vibrations in general, with a specific focus on localized nonlinearities.

Topology optimisation (TO) of continuum structures is the process of finding a sub-domain occupied by material when only the boundary conditions and loading are known [30]. In other words, it consists in finding the boundaries of a component as well as the holes present in the structure for a specific solicitation. TO is often used in a pre-design stage to identify efficient layouts of a component. Shape optimisation or parameter optimisations may be used in a second step to finely tune the shape of the component by also taking into considering other design characteristics. Different approaches can be employed to realise the TO of continuum structures. The approach used in this work is the Kriging-assisted Level-Set Method (KG-LSM) proposed by Raponi et al. [31,32,33]. It is based on the Moving Morphable Component (MMC) framework proposed by Guo et al. [34,35] coupled with the Efficient Global Optimisation (EGO) for the optimisation part [31,32,33, 36], as it has shown promising capabilities for solving large problems with unknown gradients [37,33] and for nonlinear vibrations due to friction in a preliminary work [36]. The MMC approach proposes to describe the topology of a structure as the assembly of several unitary components parametrised by their location, thickness, length, and orientation. The TO problem can then be seen as the optimisation of the components parameters. In this context, each component characterises an explicit expression of a Topology Description Function (TDF) that depends only on a limited number of parameters. If in the original work, the gradients were determined and mathematical programming techniques employed for the optimisation [34,35], several works have considered the use of global optimisation techniques, as the EGO algorithm, for the solving of the optimisation problems [37,33, 36], which are particularly adapted for non-convex optimisation or when the analytical gradients are not known or too expensive to be numerically computed. Others classical methods in TO are either based on a density-based method or on a Level-Set Method. The first one is very popular as it is robust and implemented in many Finite Element Analysis software [38,39]. The case of linear vibrations has been addressed in [40,41,42], and an extension to nonlinear vibrations was proposed in [43,44] where the nonlinear resonance of a clamped-clamped beam is optimised where geometric non-linearities are considered. The beam is cut into numerous elements, whose thicknesses are optimised based on a gradient algorithm. This work opens the field of shape optimisation for structures experiencing nonlinear vibrations. This density based approach requires the sensitivity of the objective function and of the constraints w.r.t. to the mesh element densities. The second family of methods is usually called Level-Set Method (LSM) [45,46]. It relies on an implicit description of the geometry with an LSF, which is propagated and optimised by solving an Hamilton-Jacobi equation. Both of these methods (density based and LSM) require the analytical knowledge of the objective function w.r.t. to the element densities or shape sensitivities. Considering nonlinear vibrations, these sensitivities are not always known, especially in the case of friction interfaces, which drastically reduces their applicability in this context.

The objective of this work is to propose an approach to optimise the topology of underplatform dampers to identify new shapes and new features that improve damping efficiency. In this context, an approach that couples the KG-LSM method with the HBM for the topology optimisation of structures experiencing nonlinear vibrations is proposed. If the study is focused on a specific application case, this work should be regarded as a proof-of-concept to illustrate the potential that TO offers in the context of nonlinear vibrations, as the methodology could easily be extended to others applications. More concretely, the amplitude at resonance is minimised by optimising the topology of the friction damper. The nonlinear response is efficiently computed by augmenting the HBM formulation with a phase quadrature constraint to seek directly for the nonlinear resonance. Finally, generic tools are proposed to analyse and classify the obtained geometries. By doing so, mechanical and damping properties can be assessed and family of geometries compared. This makes possible the realisation of in-depth analysis on contact properties and geometrical properties that maximises damping efficiency.

The paper is organised as follows: the academic case studied is presented as well as the numerical strategy to compute the nonlinear response function; secondly, the parametrisation of the damper and the optimisation method are described; finally, the results obtained are presented and analysed in detail. Families of damper geometries are identified and classified; and their mechanical and damping properties are compared.

2 Mechanical system under study and optimisation problem presentation

In this section, the mechanical system under study is presented as well as the different modelling choices made for the contact interface. Some initial reference results obtained for the full damper (i.e. non-optimised) are also given to illustrate the dynamic of the structure and to present the optimisation problem considered.

2.1 System geometry and modal analysis

The geometry of the structure under study is shown in Figure 2(b). It is a 2D-geometry based on the UPD test rig illustrated in Figure 2(a) [11,47]. This geometry was initially designed to simulate the behaviour of a high pressure turbine and was aimed at studying the role of friction dampers on the blades dynamic and to validate the modelling and the numerical approaches for the simulation of the nonlinear vibrations of systems with friction interfaces [11] and with uncertainties [47]. The 2D-geometry of the present study is composed of two beams with platforms linked to a common base that represents a rigid disc. Only one side of the base is clamped to remain consistent with [11]. Using a 2D geometry for the present study presents two main advantages: a diminution of the computational time as the FEM will be smaller, and a reduction of the number of optimisation parameters. Moreover, the geometry of the considered rig is trivial (simple out-of-plane extrusion) and so the problem and parameters can be approximated in 2D.

The FEM of the blades is composed of 3324 8-nodes bi-quadratic plane strain elements. This choice is based on a convergence study of the mesh not presented here for the sake of concision. The structure is made of steel with a Young's modulus of 197 GPa and a density of 7800 kg/m^3. The focus is put on the first bending mode of the blades. Since there are two blades, they can be in-phase (IP) or out-of-phase (OOP). The natural frequencies of these modes are 246.73 Hz and 247.51 Hz respectively, and the mode shapes are represented Figure 3. It is worth emphasizing that they are computed without the presence of the damper, and in the frequency range of interest, the dynamics of this system can be viewed as a 2-degrees-of-freedom system. The maximum of vibration is expected at the blade tips, and only displacements at the blade 1 tip are considered in the present study (see green point in Figure 2). The periodic excitation is located at the bottom of the blade 1, in the horizontal direction (see blue point and arrow in Figure 2).

To limit the vibration levels of the blades, UPD are placed between adjacent blades, as represented in Figure 2. In real world applications, the centrifugal loading maintains the UPD in contact with the platforms. When blades vibrate, the non-null relative displacement between the damper and the blades creates friction at

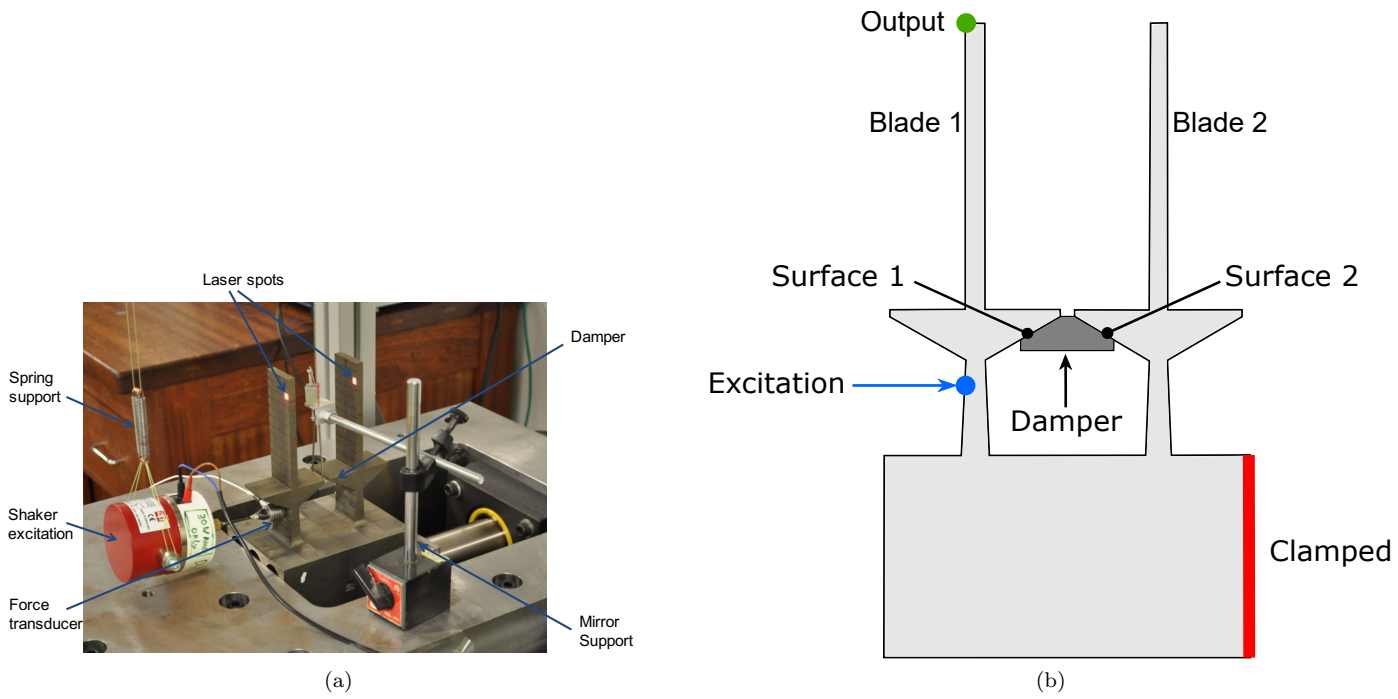

(a) (b)

Fig. 2: (a) UPD test rig [11] and (b) 2D geometry under study with the blades and the damper

the contact interfaces. Thus, energy is dissipated and the vibrations are damped. The damping performances are strongly impacted by the contact surface, and so by the damper geometry [13,18,23,25,29], justifying numerous studies on the design of this component.

The FEM of the damper is composed of 3604 8-nodes bi-quadratic plane strain elements, with the same material properties as the blades. The mesh is constructed to ensure matching between the contact points between the damper and the platforms. The number of elements for the damper might seem excessive, but it is directly related to the precision with which the geometry will be described as it will be explained later on. In the following, this damper geometry, which is the non-optimised one, will be denoted as the full damper geometry.

The friction contact interface between the damper and the platforms is the source of non-linearity in the system dynamics. One classical approach to model this friction interface consists in discretising the contact interface in many contact elements. Here, each surface is discretized into 51 2D friction contact elements. They consist of one Jenkins element and one normal spring to allow normal load variations [12]. Each contact element is defined by four parameters, namely the friction coefficient μ, the normal contact stiffness k_n, the tangential contact stiffness k_t and the normal pre-load N_0. This contact element allows for different contact states, namely stick, slip and separation, and each point can have a different status. When stick/slip occurs, energy is dissipated by friction. The illustration of the contact element as well as the expression of the contact forces are given in Appendix. The normal pre-load is assumed to be homogeneous over the contact surface and comes from [15]. It is directly related to the centrifugal loading, to the length of the contact area and to the friction coefficient. By changing the damper geometry, both the centrifugal loading and the contact area are impacted. The friction coefficient μ is set to 0.5 and the initial contact stiffness k_n and k_t are assumed equal [48].

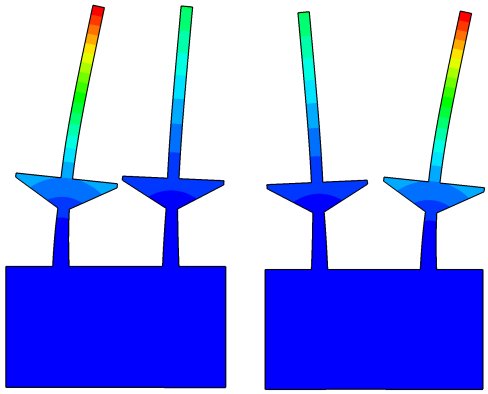

(a) $f_1 = 246.73$ Hz (b) $f_2 = 247.51$ Hz

Fig. 3: In-phase (a) and out-of-phase (b) first bending modes of the blades

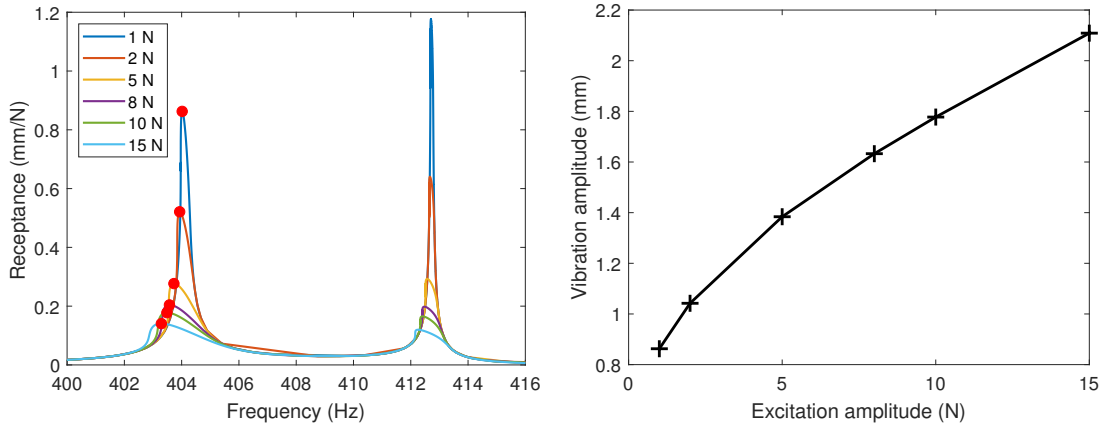

(a) (b)

Fig. 4: (a) Receptance of the forced frequency response functions for different excitation amplitude forces and (b) evolution of the vibration amplitude at the first resonance of the tip blade for different excitation levels

2.2 Reference initial forced Frequency Response Function

As an illustration, the nonlinear dynamic response obtained for the full damper is investigated first. More details about the numerical strategy to compute it will be given in Section 3.3. The forced frequency response function (FRF) for different excitation amplitude forces from 1 N to 15 N are given in Figure 4(a). As the receptance, which corresponds to the vibration amplitude divided by the excitation amplitude, is shown, the response amplitude decreases when the excitation amplitude increases. In Figure 4(b), the amplitude of vibration at the first resonance w.r.t the excitation amplitude is given. As one can see, the response amplitude is not a linear function of the excitation, illustrating the nonlinear behaviour of the problem as well as the damping introduced by the friction interface. In this case the initial contact pressure is of 9.89 N/mm. The normal and tangential contact stiffness k_n and k_t are supposed to be identical and equal to 20000 N/mm [48], and the friction coefficient

is taken equal to 0.5. The excitation is located at the bottom of the blade 1 (see the blue point in Figure 2), and the FRF is displayed for the blade 1 tip point (see the green point in Figure 2).

Looking at the FRFs, the first two resonant frequencies have largely increased because of the presence of the damper. Indeed, the IP mode resonant frequency (resp. OOP) has shifted from 246.73 Hz (resp. 247.51 Hz) to about 405 Hz (resp. 412 Hz). For both modes, when the excitation amplitude increases, the receptance decreases illustrating the nonlinear behaviour and the damping brought by the damper. For the IP mode, the receptance is divided by about 6, and the OOP peak by 8. Red points indicate where the response is in phase quadrature with the excitation for the first mode. Phase quadrature points are also observed to correspond to the points of maximum response amplitude.

Finally, the objective of the optimisation problem is to minimise this maximum of vibration reached at the first resonance by optimising the damper topology, i.e. the distribution of material in a given design domain. The vibration amplitude at the blade tip node at resonance is denoted u_{res}. As the vibration amplitudes are low, a transformation is applied in order to "spread" the objective function, so instead of optimising directly u_{res}, $y_{res} = -1/u_{res}$ is optimised. Then the optimal solution y_{res}^{opt} is solution of:

$$y_{res}^{opt} = \min_{\substack{\text{damper} \\ \text{geometries}}} y_{res} = \min_{\substack{\text{damper} \\ \text{geometries}}} -1/u_{res} \tag{1}$$

The redefinition of the objective function implies a redefinition of the domain as well, but minima are obtained for the same damper geometry. No constraints on the optimisation are considered here as the main objective is to explore all the possible geometries with interesting features and to identify interesting geometrical properties. Adding a constraint, on the volume for example, could lead to missing a class of potentially promising geometries. However, the approach remains valid when constraints are added.

3 Optimisation strategy

The goal of the optimisation problem is to optimise the damper topology to minimise the vibration levels at resonance. The general framework of the approach is described first, and then details about each step is given. It is divided into the parametrisation of the damper geometry, the computation of the nonlinear response and the optimisation process. The general framework related to the topology optimisation part is based on the Kriging-assisted Level-Set Method (KG-LSM) proposed in [33]. The approach is recalled in Sections 3.2.1, 3.2.2 and 3.4, in the following. The coupling of the KG-LSM with the HBM for the computation of the nonlinear dynamic response and the dynamic contact properties evolving within the process is developed in Sections 3.2.3 and 3.3. Moreover, specific considerations in the construction of the damper geometries are proposed as well.

3.1 General process summary

The general optimisation work-flow is summarized in Figure 5, where in Figure 5(a) the general optimisation process is described, and where in Figure 5(b) details for the objective function evaluation are presented. For each step, the section in which it is described in details is also given.

The optimisation is based on surrogate modelling, and more precisely on the Efficient Global Optimisation algorithm described in Section 3.4. The overall approach of the algorithm consists in creating a surrogate model of the objective function w.r.t. the optimisation parameters. A limited number of evaluations of the expensive objective function is computed, which defines a set of inputs and outputs, also called *Design of Experiments* (DoE). From this DoE, a cheap mathematical approximation of the objective function is build. Then, in the optimisation process, the surrogate model of the objective function is updated by adding a new point in the DoE at each iteration. The general process is stopped when a stopping criterion is reached, here a maximum

number of evaluations. The surrogate model is created by using the kriging approximation, which corresponds to the best linear unbiased estimator. The point of the design that maximizes the Expected Improvement (EI) function is added in the DoE.

Using this optimisation approach requires a parametrisation of the problem, here it means a parametrisation of the damper topology. To do so, the Moving Morphable Component (MMC) is employed and described in Section 3.2.1. Once the structural matrices of the damper are computed, the nonlinear response is computed using the Harmonic Balance Method coupled with a phase quadrature criterion to speed up the numerical simulations, described in Section 3.3. These two steps correspond to the *evaluation of the objective function* step in the workflow in Figure 5(a), and fully detailed in Figure 5(b).

3.2 Damper geometry parametrisation

3.2.1 Problem parametrisation: the Moving Morphable Components

The damper geometry is described implicitly by a Level-Set Function (LSF) [46]. Let $\mathcal{D} \in \mathbb{R}^2$ denote the bounded domain of all the admissible damper shapes. The region of $\mathcal{D}$ occupied by the material is denoted Ω. This region is described by an LSF Φ defined as:

$$\begin{cases} \Phi(\mathbf{v}) > 0 \ , \mathbf{v} \in \Omega \\ \Phi(\mathbf{v}) = 0 \ , \mathbf{v} \in \partial\Omega \\ \Phi(\mathbf{v}) < 0 \ , \mathbf{v} \in \mathcal{D} \setminus (\Omega \cup \partial\Omega) \end{cases} \tag{2}$$

where $\mathbf{v} = (v_x, v_y)^T$ is a point of the domain $\mathcal{D}$. $\partial\Omega$ is the interface between the material and the void, so the 0-iso-line defines precisely the limit between the material and the void.

The MMC framework was initially proposed by Guo et al. [34,35]. It consists in considering that the topology of a structure can be seen as an association of interconnected elementary components. Hence, each elementary component i describes a sub-domain Ω_i occupied by material. The total domain occupied by the material is the intersection of these sub-domains, i.e. $\Omega = \cup_i \Omega_i$.

Each sub-domain, and so each elementary component, is described implicitly by an LSF Φ_i. In the MMC framework, these LSF Φ_i are known explicitly, thanks to a TDF, and depend on a few number of parameters [34, 35]. Each elementary component depends on 5 parameters that characterise its position, orientation and size. By changing these parameters, one can move, rotate, shrink or expand a component. The TDF Φ_i of a component i is given by:

$$\Phi_i(\mathbf{v}) = -\left[\left(\frac{\cos\theta_i(v_x - v_x^{0,i}) + \sin\theta_i(v_y - v_y^{0,i})}{l_i/2}\right)^m + \left(\frac{-\sin\theta_i(v_x - v_x^{0,i}) + \cos\theta_i(v_y - v_y^{0,i})}{t_i/2}\right)^m - 1\right] \tag{3}$$

where $\mathbf{v} = (v_x, v_y)^T$ is a point of the domain $\mathcal{D}$. $(v_x^{0,i}, v_y^{0,i})$ is the center position of the component, θ_i its inclination with regard to the horizontal axis, l_i is its length and t_i its thickness. m is an even number, equal to 6 [33]. As an illustration, an elementary component is represented in Figure 6(a) with its parameters. The corresponding LSF is represented Figure 6(b), where all the negative values have been set to 0 for the sake of readability. The total LSF is defined as:

$$\Phi(\mathbf{v}) = \max_i \Phi_i(\mathbf{v}) \tag{4}$$

As an illustration, an assembly of three components is illustrated in Figure 6(c), where the material domain is in grey, the void in white and the 0-iso-line of the total LSF in black. By assembling elementary components, with different parameters, a complex geometry can be described. The connectivity of the final geometry is assessed by using the different LSF and by checking that there exists a continuous path between the different elementary components. In this case, geometries with isolated components are not admitted.

As this stage, the damper geometry can be described by a vector of parameters $\mathbf{p}$, which contains the properties of the different components.

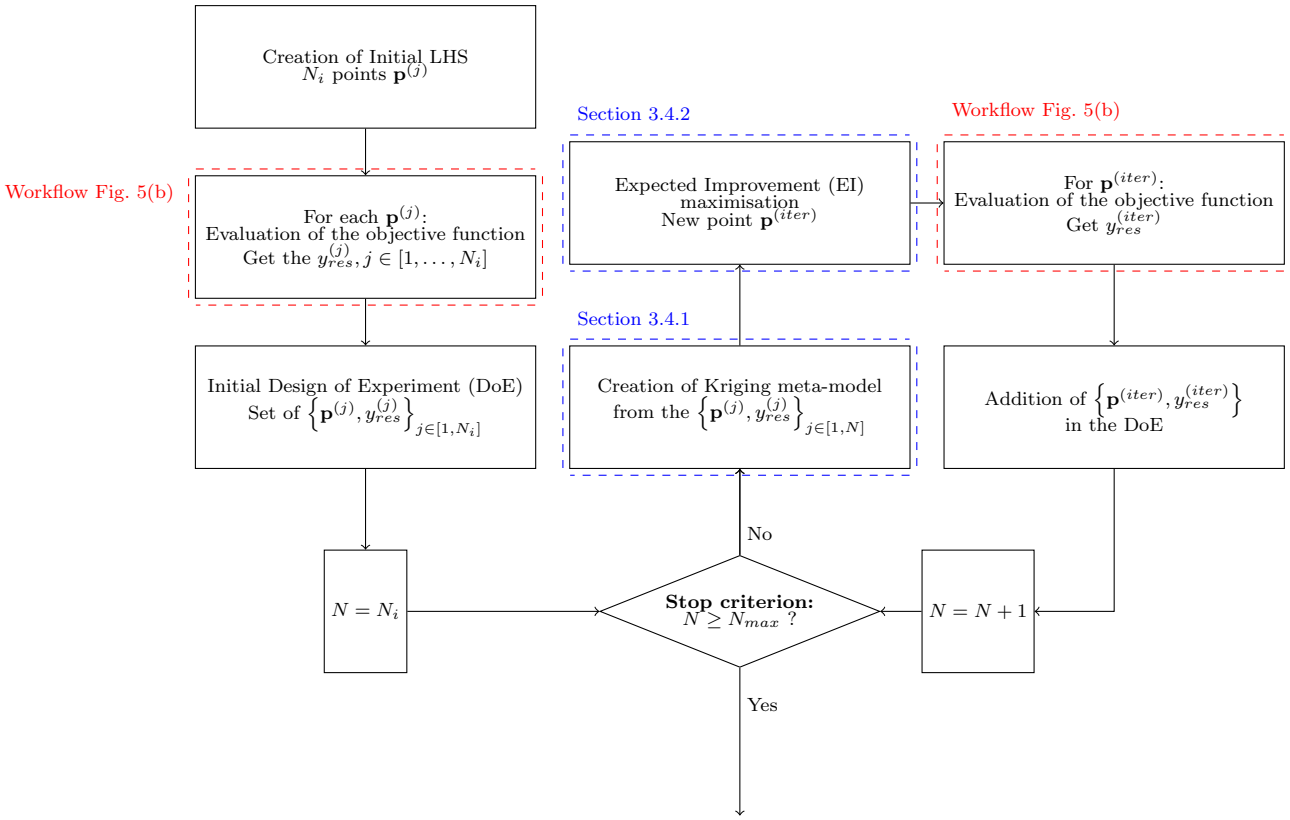

(a) Optimisation workflow

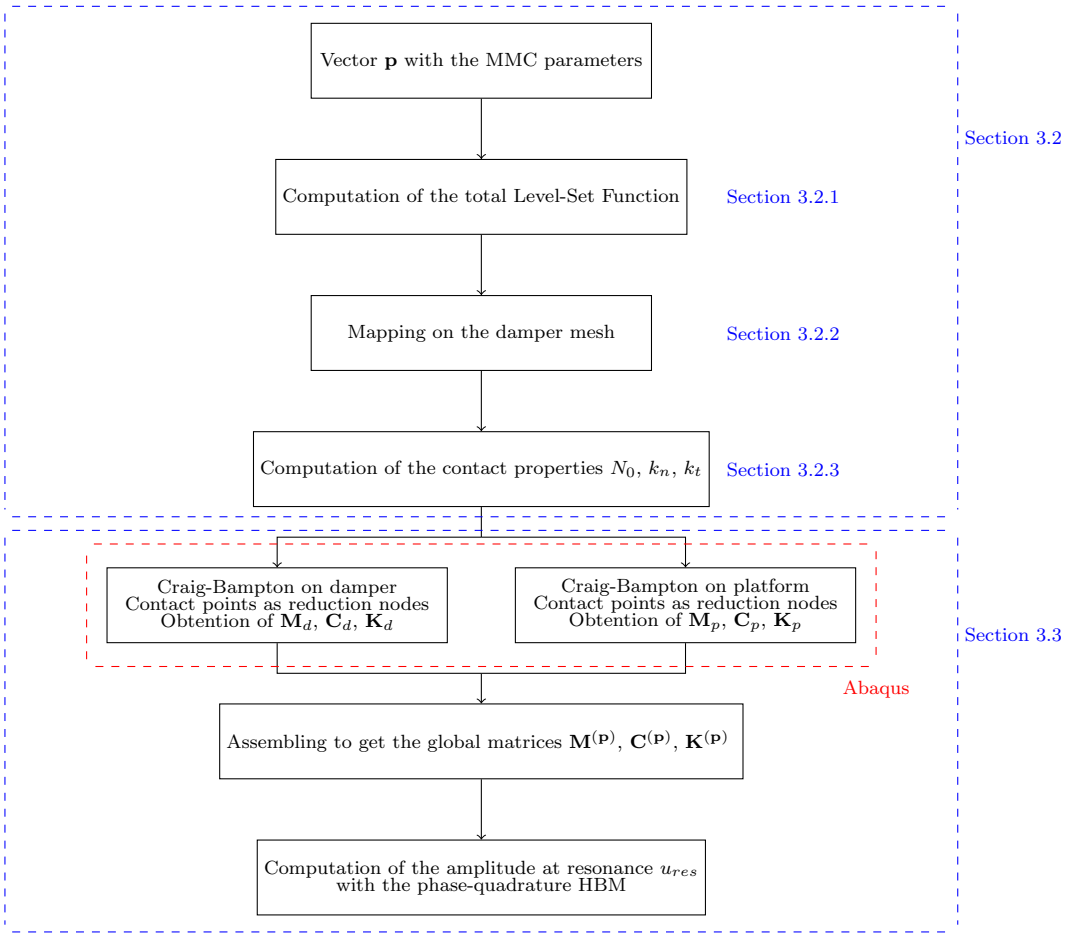

(b) Objective function evaluation

Fig. 5: General workflow of the optimisation process (a) and of the objective function evaluation (b)

3.2.2 Geometry mapping

Once the LSF is defined, the latter must be mapped on a mesh to perform the numerical simulation afterwards. In this work, a density based mapping approach [49] is adopted. It means that the LSF is translated into a density distribution over the mesh as it avoids an expensive re-meshing step [49]. More precisely:

$$\mathbf{K}_e(\mathbf{v}) = \rho(\mathbf{v})\mathbf{K}_e^0, \quad 0 \leq \rho(\mathbf{v}) \leq 1 \tag{5}$$

$$\mathbf{M}_e(\mathbf{v}) = \rho(\mathbf{v})\mathbf{M}_e^0, \quad 0 \leq \rho(\mathbf{v}) \leq 1 \tag{6}$$

where $\mathbf{K}_e^0$ is the reference stiffness matrix of a mesh element, $\mathbf{M}_e^0$ is the reference mass matrix of a mesh element and $\rho(\mathbf{v})$ is the density at $\mathbf{v} \in \mathcal{D}$. The link between the density ρ and the LSF is obtained from the Heavidise function H:

$$\rho(\mathbf{v}) = H(\Phi(\mathbf{v})) \tag{7}$$

with:

$$H(x) = \begin{cases} 1 \text{ if } x \geq 0 \\ 0 \text{ if } x < 0 \end{cases} \tag{8}$$

For numerical convenience, the LSF is discretised in the center of each element so element densities can only be equal to 0 (void) or 1 (material) [50,36]. Instead of using an ersatz material, the void elements (i.e. elements with 0 density) are then directly removed from the mesh to avoid localised modes that may appear during the modal analysis [51]. This hard kill strategy might be seen as a tough treatment. However, in the current context, only a modal analysis is done on the model and the difference in terms of natural frequencies and mode shapes is negligible, justifying this choice. It is worth noticing here that if a static analysis with stress computation was considered, then this strategy cannot be applied. With this approach, the computational time related to the mesh projection remains low and the geometry of the damper is still estimated with precision as the number of elements is high. Moreover, one could refine the mesh to increase the precision, without increasing the numerical cost. The mesh and the FEM of the damper will be used only for a modal analysis, as it will be developed in the following, and so having a rough description of the geometry as here does not have much impact on the estimation of the mode shapes and of the natural frequencies (on the condition that the mesh is fine enough to capture the geometry). The strategy is illustrated in Figure 7. The initial damper mesh is given in Figure 7(a), the 0-isolines of 5 components are given is Figure 7(b) where each color corresponds to one component and the material domain is represented in grey. The final mesh of the corresponding geometry once empty elements are

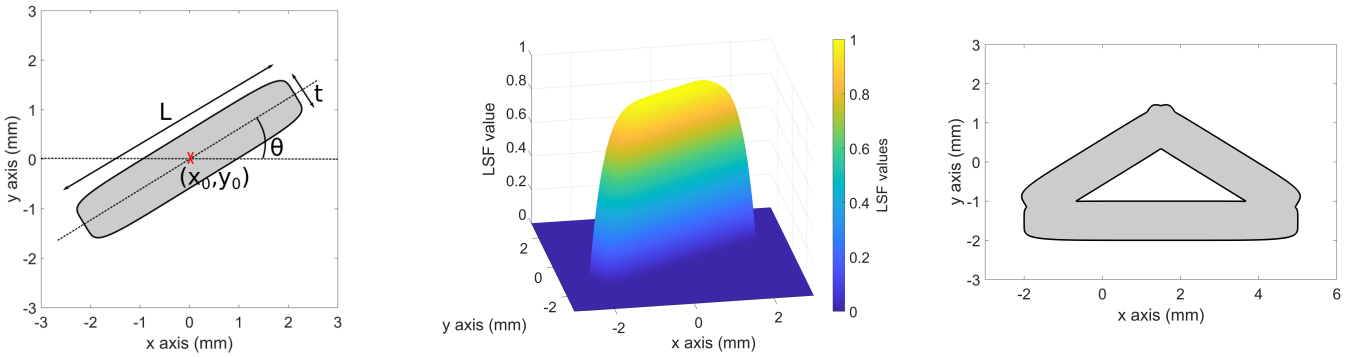

(a) (b) (c)

Fig. 6: Illustration of the MMC framework: (a) geometrical description of a component - (b) Associated Level-Set Function - (c) Assembly of 3 components - material domain in grey and void in white

235 removed is displayed in Figure 7(c).

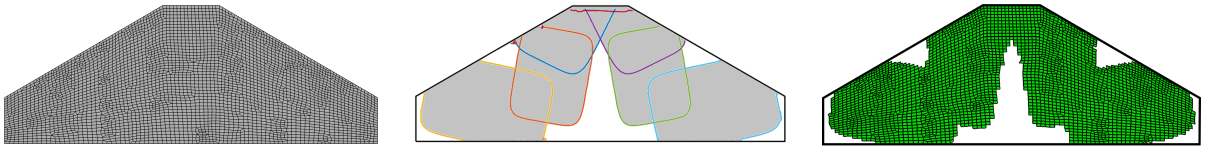

(a) (b) (c)

Fig. 7: Illustration of the LSF mapping: (a) initial damper mesh, (b) 0-isolines of the components and material domain in grey, (c) final mesh

At this step, a few geometrical constraints for mechanical and design considerations are considered

- one component is fixed and set horizontal and thin at the top of the damper to ensure the sealing of the platforms. In Figure 7(b), it corresponds to the thin horizontal bar with a burgundy 0-isoline at the top of
240 the damper.
- the damper is supposed to be symmetric about its vertical central axis so components on the right of the damper are obtained by symmetry. In Figure 7(b), the light blue component is the symmetric of the yellow one, the green component of the orange one, and the purple component of the dark blue one.
- to ensure the existence of the contact between the damper and the platforms, the center of one component
245 is imposed on the contact line (i.e. the v_x^0 and $v_y 0$ coordinates are linked for one component). In Figure 7(b), the center of the dark blue element is located on the contact line.

As this stage, for a damper geometry, and so for a given vector $\mathbf{p}$, a FEM is obtained.

3.2.3 Updating of the contact properties

During the optimisation, the damper geometry changes. This modification has an impact on the associated mechanical problem, and more precisely on the contact properties. Hence, for each new geometry, the centrifugal loading C_F and hence contact pressure changes with the mass of the damper. The new contact pressure is evaluated by considering the new centrifugal loading, but also by considering the new contact surface length that depends on the damper geometry. Considering the contact properties, the contact stiffness are also updated as they depend on the normal loading N_0 [48]. k_t and k_n as supposed to be equal and the following ratio is kept constant at each iteration, i.e. for each geometry:

$$\frac{k_n^{(1)}}{N_0^{(1)}} = \frac{k_n^{(i)}}{N_0^{(i)}} \tag{9}$$

where $k_n^{(i)}$ is the normal contact stiffness and $N_0^{(i)}$ the normal contact pressure of the geometry i.

250 3.3 Computation of the nonlinear dynamic response

The nonlinear dynamic response of the blades is computed with the Harmonic Balance Method (HBM). To reduce the computational time, a constraint on the phase is added to compute directly the resonance. The general methodology is briefly described in the following, but the interested reader may want to refer to [52,53].

The general equation of motion of the system writes:

$$\mathbf{M}^{(\mathbf{p})}\ddot{\mathbf{q}}(t) + \mathbf{C}^{(\mathbf{p})}\dot{\mathbf{q}}(t) + \mathbf{K}^{(\mathbf{p})}\mathbf{q}(t) + \mathbf{F}_{\text{nl}}^{(\mathbf{p})}(\dot{\mathbf{q}}(t), \mathbf{q}(t)) = \mathbf{F}_{\text{exc}}(t) \tag{10}$$

where $\mathbf{M}^{(\mathbf{p})}$, $\mathbf{C}^{(\mathbf{p})}$ and $\mathbf{K}^{(\mathbf{p})}$ are the mass, stiffness and damping matrix for a given damper geometry described by the vector $\mathbf{p}$, respectively. $\mathbf{q}$ is the vector of displacements and the dot represents the derivative with respect to time. $\mathbf{F}_{\text{nl}}^{(\mathbf{p})}$ is the vector of the contact nonlinear forces, which also depends on the damper geometry (number of contact points and contact properties), and $\mathbf{F}_{\text{exc}}$ is the vector of the external periodic excitation force.

A Craig-Bampton reduction is applied on the structural mass and stiffness matrices of the damper and of the platform. The number of modes retained is kept constant for numerical convenience and is taken high to ensure the quality of the reduction basis on the frequency range of interest. Finally, 12 modes are retained for the platform and 30 for the damper. The contact nodes, as well as the excitation and the output node for the platform, are retained as reduction nodes for the reduction. A Rayleigh damping of 0.001% is added on the first two structural modes of the damper and the platform for numerical stability. These different matrices are then assembled to form the global mass, stiffness and damping matrices $\mathbf{M}^{(\mathbf{p})}$, $\mathbf{K}^{(\mathbf{p})}$ and $\mathbf{C}^{(\mathbf{p})}$ respectively. These matrices depend on the damper geometry and on the number of contact nodes, and so are updated for each damper geometry. This step is performed using the Abaqus FEA software.

The underlying idea of the HBM approach consists in looking for a periodic solution and in decomposing the nonlinear dynamic response into a Fourier series. For numerical reasons, only N_h harmonic are kept and the displacements $\mathbf{q}$ can be written as:

$$\mathbf{x}(t) = \mathbf{a}_0 + \sum_{i=1}^{N_h} \mathbf{a}_i \cos(k_i \omega t) + \mathbf{b}_i \sin(k_i \omega t) \tag{11}$$

where the $(\mathbf{a}_i)$ and the $(\mathbf{b}_i)$ are the vectors of the cosine and sine Fourier coefficients respectively. The k_i are the N_h kept harmonics, and ω is the angular frequency of the solution. By injecting equation 11 in equation 10, the problem can be written in the frequency domain as:

$$\mathbf{J}_1(\mathbf{Q}, \omega) = \mathbf{Z}^{(\mathbf{p})}(\omega)\mathbf{Q} + \tilde{\mathbf{F}}_{\text{nl}}^{(\mathbf{p})}(\mathbf{Q}) - \tilde{\mathbf{F}}_{\text{exc}} = \mathbf{0} \tag{12}$$

where $\mathbf{Z}^{(\mathbf{p})}$ is the dynamic stiffness matrix of the problem, $\mathbf{Q} = [\mathbf{a}_0, \mathbf{a}_1, \mathbf{b}_1, \ldots, \mathbf{a}_{N_h}, \mathbf{b}_{N_h}]^T$ is the vector of the displacement Fourier coefficients, $\tilde{\mathbf{F}}_{\text{nl}}^{(\mathbf{p})}$ is the vector of the nonlinear contact forces in the frequency domain and $\tilde{\mathbf{F}}_{\text{exc}}$ is the vector of the excitation in the Fourier domain. They are all defined for a geometry of parameters $\mathbf{p}$. The problem described by equation 12 is solved by using a Newton-Raphson algorithm. For each iteration of the latter, an AFT procedure is employed to obtain the nonlinear contact forces in the frequency domain [54]. Inverse Discrete Fourier Transform (IDFT) and Discrete Fourier Transform (DFT) are used to alternate between the time and the frequency domains. The AFT procedure can be summarized schematically as follows:

$$\mathbf{Q}(\omega) \overset{IDFT}{\rightarrow} \mathbf{q}(t) \overset{contact}{\rightarrow} \mathbf{F}_{\text{nl}}^{(\mathbf{p})}(\dot{\mathbf{q}}(t), \mathbf{q}(t)) \overset{DFT}{\rightarrow} \tilde{\mathbf{F}}_{\text{nl}}^{(\mathbf{p})}(\mathbf{Q}) \tag{13}$$

A continuation process would be employed if the full FRF was required [36]. However, this represents a heavy computational time when only the first resonance is seek (i.e. one point in the FRF). To avoid this, the first resonance is directly aimed by adding a phase constraint between the excitation and the response. Hence, the angular frequency ω is added in the vector of unknowns. If ϕ denotes the phase between the excitation and the response, at resonance, it is equal to $\pi/2$ [55]. This is translated by adding the following constraint:

$$J_2(\mathbf{Q}, \omega) = \phi - \pi/2 = 0 \tag{14}$$

Finally, the vector of unknowns is $\boldsymbol{\zeta} = [\mathbf{Q}; \omega]$ found by solving the following problem:

$$\begin{gathered} \text{Find } \boldsymbol{\zeta} = [\mathbf{Q}; \omega] \text{ so that:} \\ [\mathbf{J}_1(\boldsymbol{\zeta}); J_2(\boldsymbol{\zeta})] = \mathbf{0} \end{gathered} \tag{15}$$

It is worth mentioning here that the phase quadrature criterion is also satisfied at the second resonance peak. To get along with this problem, several initialisations at different frequencies over a large range are done, and the results corresponding to the first peak are kept.

3.4 Optimisation method

The global optimisation method approach is based on a kriging surrogate model with the Efficient Global Algorithm (EGO) algorithm [56], for which the general workflow is given in Figure 5(a). Coupled with the MMC, it has proven to give good results for crashworthiness [33] and for nonlinear vibrations [36]. As a reminder, a kriging surrogate model is constructed and updated at each iteration of the optimisation process. This surrogate model is constructed based on a set of few evaluations of the objective function for different damper geometries. In the following, kriging meta-modelling is briefly reminded and then the EGO algorithm is presented.

3.4.1 Kriging meta-modelling

Let's consider an expensive function f of argument $\mathbf{p}$ and of value $y = f(\mathbf{p})$. A surrogate model $\widehat{f}$ of this function is a mathematical approximation of f such as: $y = f(\mathbf{p}) \approx \widehat{f}(\mathbf{p})$ constructed from a set $\left\{(\mathbf{p}^{(i)}, y^{(i)})_{i=1,\dots,N}\right\}$ of N inputs/outputs [56,57]. This DoE is generated by the user and by evaluating the function f and the points $(\mathbf{p}^{(i)})$. The kriging approach approximates the function f with [56,58]:

$$\widehat{f}(\mathbf{p}) = \sum_{j=1}^{q} \alpha_j g_j(\mathbf{p}) + \mathcal{Z}(\mathbf{p}) \tag{16}$$

where the g_j are q-real known functions, $\boldsymbol{\alpha}$ is a vector of coefficients to be determined and $\mathcal{Z}$ is a zero-mean Gaussian process of unknown variance σ^2. The covariance function is given by $C(\mathbf{p}, \mathbf{p}') = \sigma^2 \mathcal{R}(\mathbf{p}, \mathbf{p}')$, where $\mathcal{R}$ is the known correlation function. The functions g_i are chosen *a priori* depending on the knowledge of the phenomena to model, and are often polynomials of low order (0, 1 or 2). The correlation function $\mathcal{R}$ is usually unknown and so is constructed from a family of kernel functions that depend on a parameter $\boldsymbol{\theta}$, solution of an optimisation problem [58].

The mean prediction at an input $\mathbf{p}_0$ is given by:

$$\widehat{f}(\mathbf{p}_0) = \widehat{y}_0 = \mathbf{g}_0^T \widehat{\boldsymbol{\alpha}} + \mathbf{r}_0^T \mathbf{R}^{-1} (\mathbf{y} - \mathbf{G}\widehat{\boldsymbol{\alpha}}) \tag{17}$$

and the variance is given by:

$$s^2(\mathbf{p}_0) = \sigma^2 \left(1 - \mathbf{r}_0^T \mathbf{R}^{-1} \mathbf{r}_0 + \left(\mathbf{g}_0 - \mathbf{G}^T \mathbf{R}^{-1} \mathbf{r}_0\right)^T \left(\mathbf{G}^T \mathbf{R}^{-1} \mathbf{G}\right)^{-1} \left(\mathbf{g}_0 - \mathbf{G}^T \mathbf{R}^{-1} \mathbf{r}_0\right)\right) \tag{18}$$

where $\mathbf{R}$ is the correlation matrix whose coefficients are $R_{ij} = C(\mathbf{p}^{(i)}, \mathbf{p}^{(j)})$, $\mathbf{G}$ is the regression matrix of coefficients $G_{ij} = g_j(\mathbf{p}^{(i)})$, $\mathbf{g}_0$ is the vector of $g_j(\mathbf{p}_0)$ and $\mathbf{r}_0$ is the vector of $C(\mathbf{p}_0, \mathbf{p}^{(i)})$. One can notice that at the learning points, the predictions are exact and the variance is null. Moreover, the variance depends only on the input points, and not on the output. For more details on the mathematical background and the practical construction of such surrogate models, the interested reader could refer to [56,58].

3.4.2 Efficient Global Optimisation algorithm

The Efficient Global Optimisation (EGO) algorithm is an algorithm proposed by Jones at al. [56] to perform optimisation with kriging. It is an iterative approach where points are added one by one in the DoE. A kriging surrogate model of the objective function is constructed at each iteration based on the current DoE and is exploited to find the new point to be added in the DoE. The latter are added one by one and are selected based on the Expected Improvement (EI) criterion. This criterion presents a good compromise between space exploration and minimum exploration. In the present case, this EI is slightly modified to deal with the unconnected geometries and a penalty is considered for the infeasible configurations [33]. This modified EI is defined as:

$$EI(\mathbf{p}) = \begin{cases} (y^+_{min} - \widehat{f}(\mathbf{p}))\Phi\left(\frac{y^+_{min}-\widehat{f}(\mathbf{p})}{s(\mathbf{p})}\right) + s(\mathbf{p})\phi\left(\frac{y^+_{min}-\widehat{f}(\mathbf{p})}{s(\mathbf{p})}\right) & \text{if connected geometry} \\ 0 & \text{if connected geometry and s}(\mathbf{x}) = 0 \\ -P * \gamma & \text{if non-connected geometry} \end{cases} \tag{19}$$

where y^+_{min} is the best minimum found so far, Φ is the cumulative density function of the normal law and ϕ the probability density function of the normal law. P is evaluated only when the geometry is not connected, and is the minimal distance between the different components computed based on a 2D-graph [33], and γ is a constant factor, equal to 1000 here. At each iteration, for the point $\mathbf{p}_{new}$ solution of:

$$\mathbf{p}_{new} = \max_{\mathbf{p}} EI(\mathbf{p}) \tag{20}$$

the evaluation of objective function is performed, i.e. $f(\mathbf{p}_{new})$ is computed, and $\{(\mathbf{p}_{new}, f(\mathbf{p}_{new})\}$ is added in the DoE. To solve this problem, the R-genoud algorithm is employed and combines a genetic algorithm with a BFGS algorithm [59]. The gradient of the EI is given by [58]:

$$\nabla EI(\mathbf{p}) = -\nabla\widehat{f}(\mathbf{p}) \times \Phi\left(\frac{y^+_{min} - \widehat{f}(\mathbf{p})}{s(\mathbf{p})}\right) + \nabla s(\mathbf{p}) \times \phi\left(\frac{y^+_{min} - \widehat{f}(\mathbf{p})}{s(\mathbf{p})}\right) \tag{21}$$

when the geometry is connected and is computed by finite difference otherwise.

4 Results and discussion

4.1 Case presentation

Five components are used to describe the damper geometry, which would represent $5 \times 5 = 25$ optimisation parameters. With the considerations explained in Section 3.2.1, the final optimisation problem is of dimension 9. The minimal and maximal physical values of each variable is given in Table 1. In the optimisation process, they are mapped to the $[0, 1]$ interval. For practical and numerical reasons, instead of controlling θ_i for the inclination of the component, $\sin\theta_i$ is controlled and $\cos\theta_i$ is defined as $\sqrt{1 - \sin^2\theta_i}$.

An initial LHS of 200 points is generated for the DoE creation and non-connected geometries are removed [33]. The final DoE is composed of 55 points. For the kriging construction, a Matérn 5/2 kernel and a constant trend are taken [58]. The optimisation of the friction damper geometry is stopped after 200 iterations. The choice

Parameter	**Length L (mm)**	**Thickness t (mm)**	**Orientation θ (rad)**	**x position (mm)**	**y position (mm)**
min value	1	1	$-\pi/2$	0	0
max value	30	20	$\pi/2$	20.4	15

Table 1: Range of variation of the optimisation parameters

of a maximum budget of 200 evaluations is based on a convergence study performed on several cases and for different initial DoE. It appears that 200 evaluations was a good compromise, as improvement of the objective function afterwards was negligible.

4.2 Optimisation results

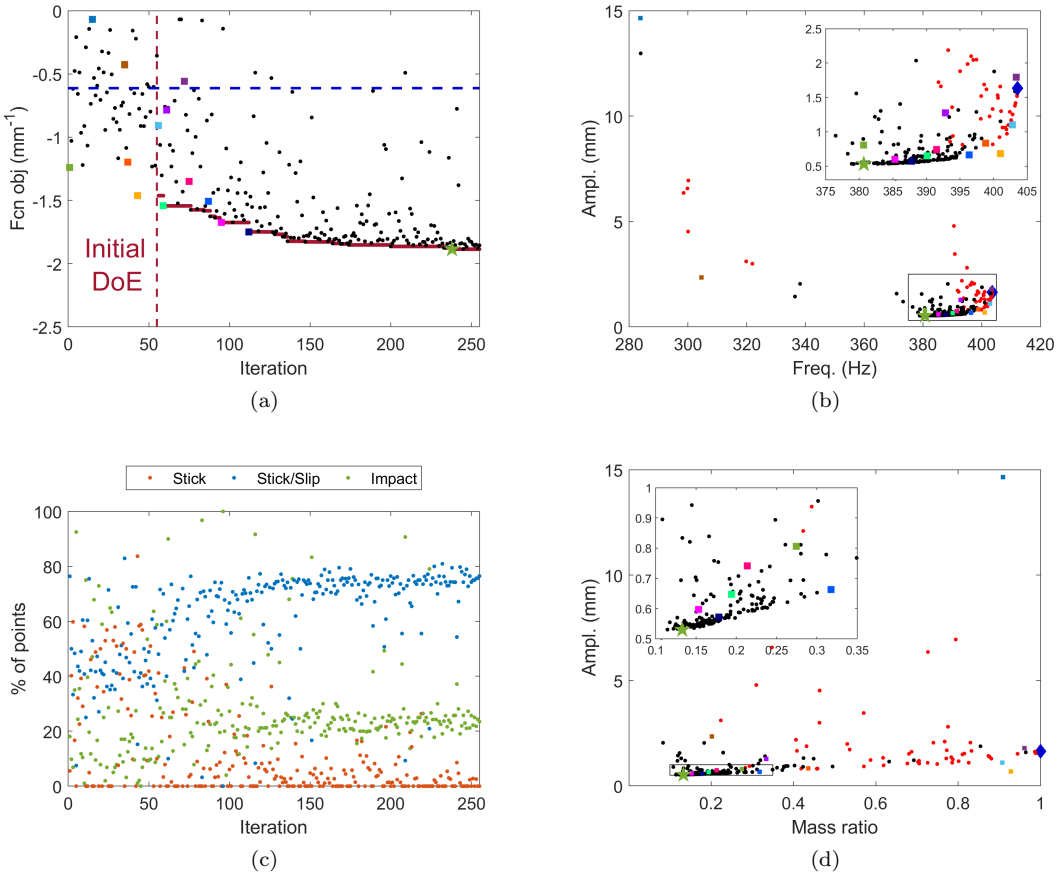

Fig. 8: (a) Evolution of the objective function vs iterations where red dots are the current minimum at each iteration and (- - -) the full damper case - (b) Amplitude at resonance vs resonance frequency of the different configurations - (c) Repartition of the contact status vs iterations - (d) Amplitude at resonance vs mass ratio - (●): initialisation points - (■): displayed geometries - (★) best geometry - (♦): full damper

Optimisation results are given in Figure 8. In Figure 8(a), the evolution of the objective function versus the evaluation number is given where the first 55 evaluations correspond to the initial DoE. Black points correspond to the value of the objective function for the considered geometry and red points correspond to the current minimum at each iteration in the optimisation process (i.e. it corresponds to y^+_{min} in Equation 19). The blue dashed line corresponds to the full damper case. The best result is marked with a green star, and a few particular geometries are marked with coloured squares and displayed in Figure 9. In the initial DoE, the

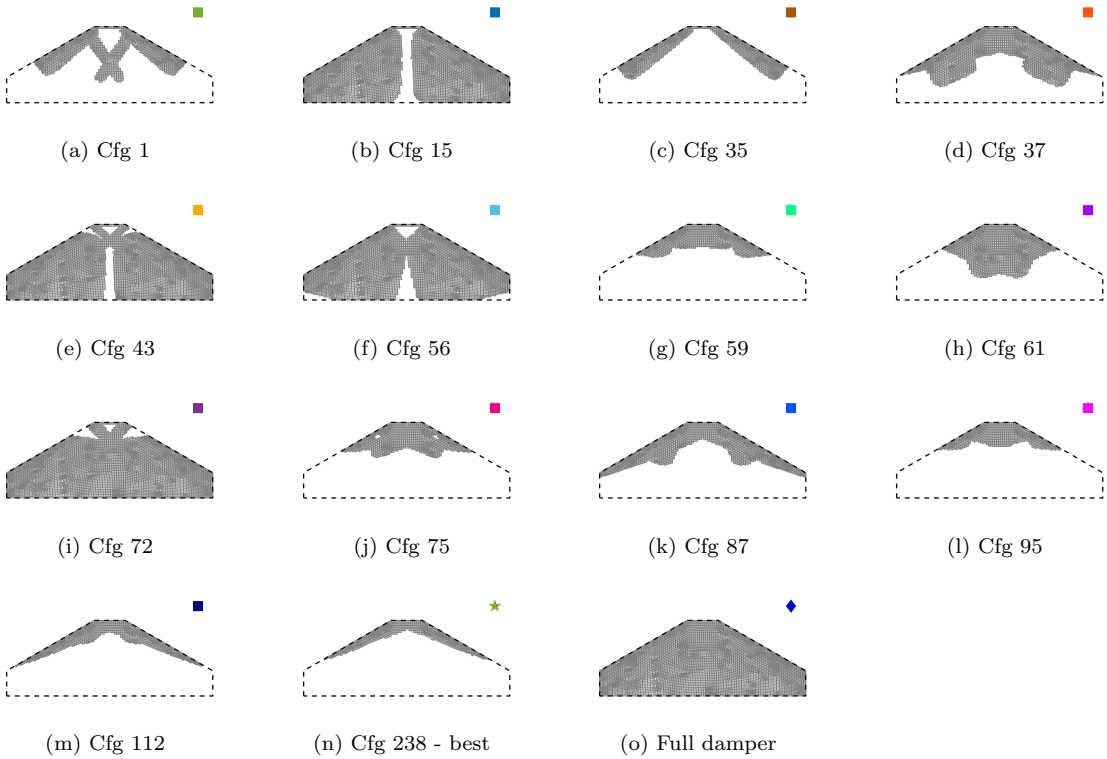

(a) Cfg 1 (b) Cfg 15 (c) Cfg 35 (d) Cfg 37

(e) Cfg 43 (f) Cfg 56 (g) Cfg 59 (h) Cfg 61

(i) Cfg 72 (j) Cfg 75 (k) Cfg 87 (l) Cfg 95

(m) Cfg 112 (n) Cfg 238 - best (o) Full damper

Fig. 9: Illustration of some damper geometries

objective function takes value between -1.46 mm^{-1} (i.e. 0.68 mm) and -0.068 mm^{-1} (i.e. 14.7 mm). The best geometry found so far is given in Figure 9(e) and the worst one in Figure 9(b). In Figures 9(a-e), one can see the large variety of damper shapes in the initialisation, with more or less mass and with different topologies. Over the optimisation, new minima are found iteratively and the objective function takes smaller and smaller values and the points are less and less spread and take values near the current minimum (see black points grouped around the red points). The best value found over the 200 iterations is reached at iteration 183 and is equal to -1.88 mm^{-1} (0.53 mm), and the corresponding geometry is given in Figure 9(n). Compared to the initial DoE, it corresponds to an improvement of 28% of the objective function, and a reduction of 22% of the vibration level. T he second resonance peak for the OOP mode, as the amplitude has been cut down from 1.58 mm to 0.7 mm. Both resonance peaks have been shifted considerably on the right. The first resonance peak experiences a shift of 22.9 Hz, and the second a shift of 10.3 Hz. Moreover, both peaks show a more pronounced softening behaviour, especially the first peak. The interest of such approach is obvious.

Over the optimisation, the geometries associated to new minima are more and more similar. In Figures 9(g,l,m,n) some of these geometries are given. The algorithm converges progressively to a shape similar to a $\wedge$ with a spread contact surface and thin branches. This shape is completely different from the shapes present in the initialisation, which illustrates the capacity of the algorithm to identify new geometries. Moreover, at the beginning of the optimisation, new minima are found regularly but after iteration 125 this is rarer and the improvement is marginal.

For more insights, some mechanical and dynamics properties are also extracted. In Figure 8(b) the resonance amplitude w.r.t the resonance frequencies is given for the different tested geometries (red points are the 55 initialisation points), in Figure 8(c) the repartition of the contact status at resonance are given and in Figure 8(d)

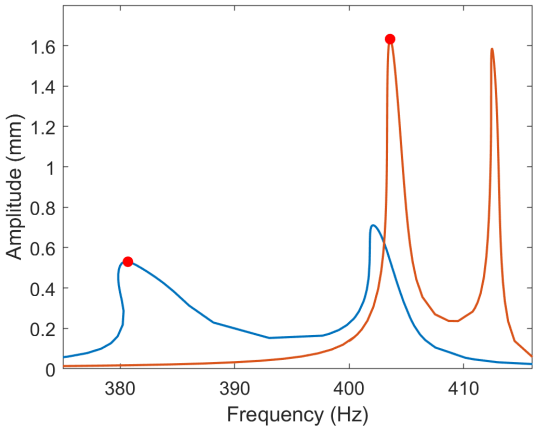

Fig. 10: Comparison of the FRF at the tip blade for the full damper (orange) and for the optimised damper (blue) - (•): solution obtained with the phase quadrature criterion

	Full damper	**Best geometry**
Mass ratio	1	0.13
Vib. amp. (mm)	1.63	0.53
Res. freq. (Hz)	403.57	380.68

Table 2: Comparison of resonance properties of the full and the optimised dampers

the resonance amplitude w.r.t the mass ratio (i.e. ratio between the mass of the damper and the mass of the full damper) are given (red points are the initialisation points). The coloured squares correspond to the specific geometries given in Figure 9.

Looking at the resonance frequencies in Figure 8(b), in the large majority of cases, the resonance frequency is between about 378 Hz and 403 Hz. Some geometries have much lower resonance frequencies up to about 280 Hz, two of them are illustrated in Figure 9(b,c). They correspond to geometries with a too high flexibility as only the component present to seal the platforms ensure the connection between the right and the left part of the damper. This brings a more linear behaviour, and so the resonance frequency is less shifted and vibrations are less damped (and so the amplitudes tend to increase to infinity as no other source of damping is present in the model). For the other cases (see the zoom in Figure 8(b)), a reduction of the resonance amplitude corresponds to a decrease of the resonance frequency and the different tested cases describe a circular arc. The best geometry has a resonance frequency of 380.7 Hz, when the full damper has a resonance frequency of 403.5 Hz. This represents a variation of about 5%. Geometries corresponding to points on the circular arc are given in Figure 9(d,f,i,k,n). They have various and more or less complex geometries as one can see. If the geometries (i,f,d) are not extremely efficient is terms of damping, the geometry (k) have level of vibrations that could be acceptable and be an alternative to the optimised shape (n). If the resonant frequency also becomes a design criterion, then the geometries (g,j,m) present an alternative with slightly higher vibration levels but a higher resonance frequency. Looking at the impact of the mass on the resonance amplitude in Figure 8(d), the optimised geometry present a drastic reduction of the damper mass as the mass ratio is equal to 0.13. The initialisation points (see red dots) are spread over the mass ratio, but optimisation points are more located on lower mass. This shows that minimising the amplitude tends to also reduce the damper mass. However, having similar mass does not imply similar damping efficiency as with high mass, the damper can be efficient or not (see the geometry (e) versus the geometry (b)), and similar conclusions can be drawn for low mass dampers (see (c) vs (g)). For a more global overview, the objective function versus the resonance frequency and the mass ratio are displayed in a 3D plot in Figure 11, red points are the initialisation points. The algorithm globally converges to the optimised geometries.

Finally, the repartition of the contact status for each geometry is given in Figure 8(c). It correspond to the percentage of contact points in a stuck, stick/slip status or experiencing impact at resonance. For the

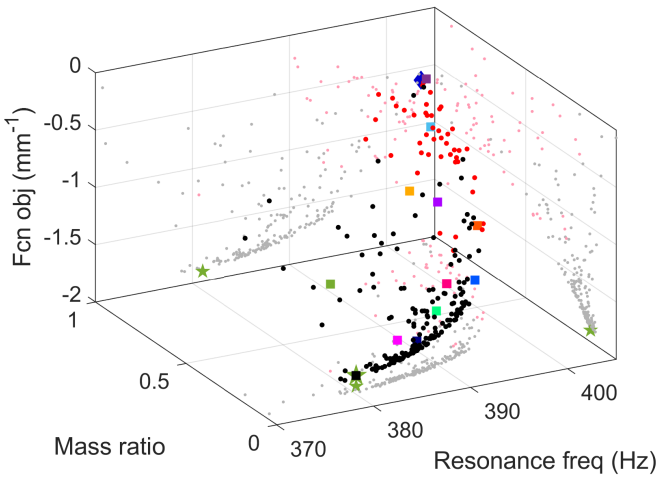

Fig. 11: 3D graph of the objective function vs the mass ratio vs the resonance frequency of the tested geometries - (●): initialisation points - (■): displayed geometries - (★) best geometry - (♦): full damper

initialisation geometries, the contact behaviours are various. But during the optimisation, after a only few iterations, most geometries have about 80% of their contact points that experience stick/slip, almost zero points are in stuck position and about 20% of the points experience impact. As the damping is generated by the stick/slip motion, points that are in a stuck position does not provide damping and are avoided in the optimisation. Impact is a well-known behaviour for wedge damper [23], that cannot be avoided with this type of geometry. However, even if a point experience impact, it is not experienced during the full vibration period and so on some stick/slip can still takes place and so provides some damping. So by optimising the vibration levels, geometries that have points in stuck status tend to be avoided.

4.3 Geometries analysis

To extrapolate and provide a more in-depth analysis, geometries are clusterised. First, a distance definition is chosen. If $\mathbf{v}_{grid} = \left\{\mathbf{v}^{(k)}\right\}$ denotes the coordinates of the mesh element centres where the LSF $\Phi_{\mathbf{p}}$ related to the damper geometry defined by the parameter vector $\mathbf{p}$ is evaluated, then the following function $G_{\mathbf{p}}$ is defined:

$$G_{\mathbf{p}}(\mathbf{v}^{(k)}) = \begin{cases} 1 & \text{if } \Phi_{\mathbf{p}}(\mathbf{v}^{(k)}) > 0 \\ 0 & \text{if } \Phi_{\mathbf{p}}(\mathbf{v}^{(k)}) \leq 0 \end{cases} \tag{22}$$

The distance d between two geometries defined by the vectors $\mathbf{p}$ and $\mathbf{p}'$ is then given by:

$$d(\mathbf{p}, \mathbf{p}') = \sqrt{\sum_k \left(G_{\mathbf{p}}(\mathbf{v}^{(k)}) - G_{\mathbf{p}'}(\mathbf{v}^{(k)})\right)^2} \tag{23}$$

The vectors $\mathbf{p}$ and $\mathbf{p}'$ are not directly taken are geometries can be similar or identical with different MMC parameters (components switched, superimposed etc). By taking directly the LSF values, similar problem can happen as the value of the LSF can vary, but not the geometry.

In order to get a general overview on the distance between the different damper geometries, the distance matrix $\mathbf{D}$ which coefficients are $D_{i,j} = d(\mathbf{p}^{(i)}, \mathbf{p}^{(j)})$ where $\mathbf{p}^{(i)}$ and $\mathbf{p}^{(j)}$ are the i*th* and j*th* geometries. The matrix entries are normalized by dividing by the maximum observed distance. The final matrix is given in Figure 12. If

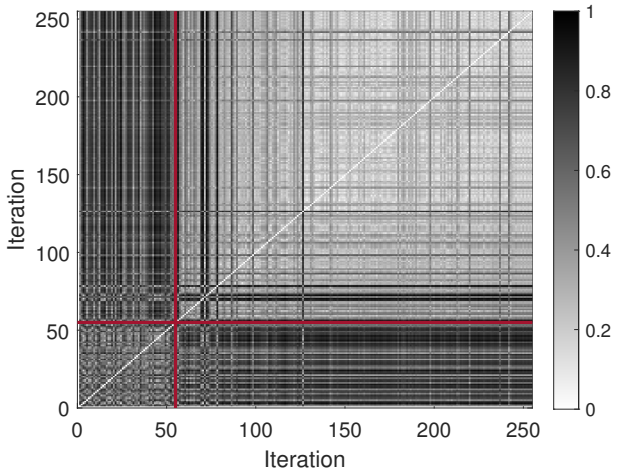

Fig. 12: Distance matrix between the different geometries - (—) limits of the initial DoE

a value is close to one then the geometries are very different (i.e. many mesh elements are present in one and not the other), and if a value is equal to 0 then the geometries are very close. From the matrix, it can be first seen that the 55 initial geometries are very different from one to another and are very different from geometries observed during optimisation as the distance values are relatively high. During the optimisation, at the beginning, some very different geometries are tested (see the black lines around iteration 70) but progressively the geometries are more and more similar as the distance values are getting lower and lower. This indicator must however be taken with caution as it is an indicator of the similarity of empty and full elements, and not an indicator of the geometry in itself. So, if two geometries are similar from a visual perspective, but if one of them is an homothety of the other then the distance can be relatively high whereas the geometries could be considered as similar.

The different damper geometries are finally clusterised to be classified. To do so, geometries observed regularly in the results are taken as reference for the creation of different clusters. Geometries that have a normalised distance inferior to 0.2 from a reference geometry are grouped in the same cluster. To compensate the homothety issue, for one cluster several geometries can be taken as reference and any geometry close enough from one of them is group in the cluster. A distance of 0.2 proved to be a good compromise to filter the geometries, but a visual check was still performed and some rare outliers were sometimes removed of a cluster. Finally, five clusters are retained and their main characteristics are summarized in Table 3. For each cluster, the size of the cluster, the geometrical property are given as well as the mean and the variance of the resonance amplitude, the resonance frequency and the mass ratio. Thus, Cluster 1 is characterised by geometries that have two large masses on the side, Cluster 2 by geometries that have a $\wedge$ shape, Cluster 3 by geometries that are flat at the bottom, Cluster 4 by geometries that have a clear central hole and Cluster 5 by geometries that have a central bump. A representative geometry of each cluster is given in Figure 13. It is worth emphasizing here that the cluster notion here is only a tool to analyse and group the results to see if one geometry seems more appropriate than another and present interesting features. Indeed, the limit between two clusters is thin and some specific geometries could be put in two clusters. From the results, one can see that the cluster 2 has a low variance for all properties and so the shape is robust to a variation of its geometry. On the opposite, for the Cluster 1, the variance is high and so a modification of the geometry can lead to large variation of the dynamic properties. The average and the variance of the initial pressure and of the contact status distribution are summarized in Table 4 for each cluster. Cluster 5 has the highest initial pressure on average, which can be related to the relatively higher damper mass in this cluster, and Cluster 2 has the lowest initial pressure. Considering the contact condition, Cluster 4 and Cluster 5 have geometries were the highest amount of stick condition is experienced (9.7% and 11.6% on average, resp.). The first three clusters have, on the opposite, a low ratio of contact points

Cluster	Geom. carac	Nb cfg	Ampl (mm)		Mass ratio		Res. freq (Hz)	
			mean	variance	mean	variance	mean	variance
1	Bump on sides	33	1.28	4.49	0.23	5.9E-3	381.64	417.22
2	$\wedge$ shape	123	0.58	6.7E-3	0.17	3.0E-3	387.45	14.62
3	Flat	15	1.19	2.63	0.19	8.7E-3	387.97	46.67
4	Central hole	15	0.79	0.13	0.25	6.3E-3	389.45	210.72
5	Central bump	5	1.18	0.27	0.29	0.01	392.82	15.07

Table 3: Dynamic and mechanical properties of the different geometry clusters

Cluster	Geom. carac	Nb cfg	N_0 (N)		% stick		% impact		% stick/slip	
			mean	variance	mean	variance	mean	variance	mean	variance
1	Bump on sides	33	3.37	0.37	1.9	7.6	36.1	298.7	61.9	258.3
2	$\wedge$ shape	123	2.37	0.29	3.4	26.9	23.5	39.2	73.1	40.8
3	Flat	15	3.51	0.63	4.9	87.7	42.7	689.5	52.3	516.2
4	Central hole	15	3.32	0.73	11.6	82.3	27.3	492.9	61.1	318.3
5	Central bump	5	5.16	1.67	9.7	196.8	47.6	851.2	42.6	391.6

Table 4: Contact properties of the different clusters

in a stick state (up to 5% maximum). Considering the ratio of contact points experiencing impact, it is higher for Cluster 3 and Cluster 5, with 42% and 47% of points experiencing impact, respectively. But all geometries experience some impact (lowest value equal at 23% for the Cluster 2). Finally, the second cluster has the highest amount of contact points in stick/slip condition (about 73%), whereas the other clusters have less points in this status. It can go down to 42% for the Cluster 5. So by optimising purely the maximum amplitude, geometries that tend to maximise the amount of stick/slip are selected. This tends to be obtained by having a low initial contact load (see low value for N_0 for the Cluster 2) and a larger number of contact points to distribute this load, and thus avoiding stuck conditions. Indeed, the Clusters 1, 3, 4 and 5 have a larger initial pressure and less contact points, pushing back the starting of stick/slip. As the normal load N_0 is directly proportional to m/l with m the damper mass and l the length of the contact surface, reducing N_0 is achieved by reducing the damper mass and by increasing the contact surface. This is directly translated by the $\wedge$ geometry and the two long and thin branches. As the normal load is low, contact points enter stick/slip more easily and so more damping is provided.

If these results are in accordance with what we could expect, it also raises an important point. The results are strongly related to the modelling choices. One could easily see one of the limitation of TO here, as by changing slightly a modelling choice, one could expect a completely different TO result. From the other way round, if the modelling is approximative, then the result of TO might not be optimised for the real case. This illustrates that TO remains a tool, but results must be taken with caution and the modelling must be as close as possible from the real system, which might be a problem when many uncertainties are present. Another important point is the restriction of the design space introduced by the MMC framework and the geometry constraints considered here (symmetry for e.g.). Indeed, as the number of components is low here, numerous geometries are not in the design space, as geometries with bumps on the contact line or non-symmetric ones. So, the optimal geometry found here might not be the real optimal one. However, despite these restrictions, results are promising and demonstrates the interest of such an approach.

5 Conclusion

A numerical strategy for the optimisation of the topology of friction dampers to mitigate the level of vibrations at resonance has been proposed in this study. The demonstration has been proposed on an academic 2D case

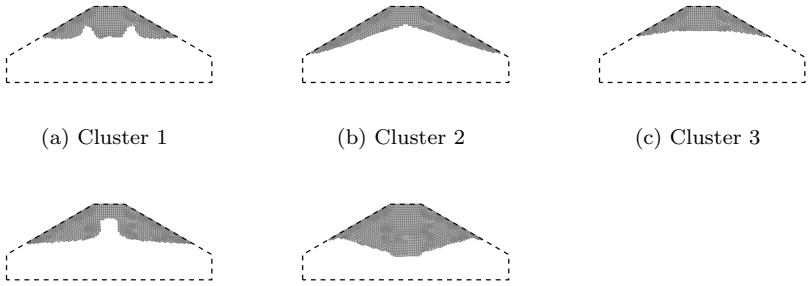

(a) Cluster 1 (b) Cluster 2 (c) Cluster 3

(d) Cluster 4 (e) Cluster 5

Fig. 13: Representation of a representative geometry of each cluster

composed of a two blades system and one damper. The damper topology is directly parametrised by using the Moving Morphable Components framework. The latter reduces drastically the number of optimisation parameters, and more traditional global optimisation methods can be employed. In this work, the Efficient Global Optimisation algorithm is employed, by iteratively adding points in the DoE, the kriging surrogate model of the objective function is updated. The presence of the contact interface makes the system nonlinear, and the nonlinear dynamic response is computed with the well-known Harmonic Balance Method. To reduce the computational cost, a phase quadrature criterion is added in the formulation to directly seek for the resonance peak. By this approach, the full FRF doesn't have to be computed, reducing the numerical cost.

Results show that in few iterations and with a limited number of simulations, efficient damper geometries are obtained with interesting features. The algorithm focuses quickly on the most efficient shapes. However, as many geometries are tested, access to other geometries with other characteristics is possible. The obtained geometries are clustered for a more in-depth analysis. Results show that a geometry that reduces the initial normal pressure at the contact interface (by reducing the mass) and that increases the contact surface are preferable as it leads to more points stick/slip on the contact surface.

If the results are encouraging, more work on the topic should be conducted in the future. First, if the MMC framework reduces drastically the number of optimisation parameters, it is also the main drawback of the method as the design space is limited. This could be handled by considering either more components, or components with more complex shapes. However, this represents an increase in the number of optimisation parameters, which could lead quickly to the maximum number of parameters kriging can handle, and other optimisation strategy might be required. Indeed, in global optimization methods, especially with kriging, the number of optimization parameters that the algorithm can handle is quickly limited (typically up to about 15 for kriging). To consider larger applications (as 3D), this will be a real limitations and other optimisation algorithm must be investigated.

Finally, realistic constraints should be added in the optimisation, in particular to consider the mechanical integrity and the consistent manufacturability of the damper. Moreover, numerous uncertainties are present in the model, especially for the contact, and robust optimisation should be considered. And last but not least, an extension to the 3D should be considered to apply the method to more realistic blade modelling.

Acknowledgements E. Denimal and L. Salles have received funding from Rolls-Royce and the EPSRC under the Prosperity Partnership Grant CornerStone (EP/R004951/1). L. Renson has received funding from the Royal Academy of Engineering (RF1516/15/11). Rolls-Royce, the EPSRC and the Royal Academy of Engineering are gratefully acknowledged.

Conflict of interest

The authors declare that they have no conflict of interest.

Replication of results

Replication of the computational results is possible with simulation algorithm and parameters presented Sections 2 and 3. Code and data for replication can be provided by the corresponding author up on reasonable request.

References

1. J. Griffin. A review of friction damping of turbine blade vibration. *International Journal of Turbo & Jet-Engines*, 7(3-4):297–308, 1990.
2. B. Feeny, A. Guran, N. Hinrichs, and K. Popp. A Historical Review on Dry Friction and Stick-Slip Phenomena. *Applied Mechanics Reviews*, 51(5):321–341, 05 1998.
3. L. Gaul and R. Nitsche. The Role of Friction in Mechanical Joints. *Applied Mechanics Reviews*, 54(2):93–106, 03 2001.
4. EP Petrov and DJ Ewins. State-of-the-art dynamic analysis for non-linear gas turbine structures. *Proceedings of the Institution of Mechanical Engineers, Part G: Journal of Aerospace Engineering*, 218(3):199–211, 2004.
5. M. Krack, L. Salles, and F. Thouverez. Vibration prediction of bladed disks coupled by friction joints. *Archives of Computational Methods in Engineering*, 24(3):589–636, 2017.
6. BA Cowles. High cycle fatigue in aircraft gas turbines—an industry perspective. *International Journal of Fracture*, 80(2):147–163, 1996.
7. M. Berthillier, C. Dupont, R. Mondal, and J. J. Barrau. Blades Forced Response Analysis With Friction Dampers. *Journal of Vibration and Acoustics*, 120(2):468–474, 04 1998.
8. K. Sanliturk, D. Ewins, and AB Stanbridge. Underplatform dampers for turbine blades: theoretical modeling, analysis, and comparison with experimental data. *J. Eng. Gas Turbines Power*, 123(4):919–929, 2001.
9. K. Sanliturk, D. Ewins, R. Elliott, and J. Green. Friction damper optimization: simulation of rainbow tests. *J. Eng. Gas Turbines Power*, 123(4):930–939, 2001.
10. J Szwedowicz, C Gibert, TP Sommer, and R Kellerer. Numerical and experimental damping assessment of a thin-walled friction damper in the rotating setup with high pressure turbine blades. *Journal of Engineering for Gas Turbines and Power*, 130(1), 2008.
11. L. Pesaresi, L. Salles, A. Jones, J.S. Green, and C.W. Schwingshackl. Modelling the nonlinear behaviour of an underplatform damper test rig for turbine applications. *Mechanical Systems and Signal Processing*, 85:662–679, 2017.
12. EP Petrov and DJ Ewins. Analytical formulation of friction interface elements for analysis of nonlinear multi-harmonic vibrations of bladed disks. *J. Turbomach.*, 125(2):364–371, 2003.
13. L. Panning, W. Sextro, and K. Popp. Optimization of interblade friction damper design. volume 4, 2000.
14. M. Jareland. A parametric study of a cottage-roof damper and comparison with experimental results. volume 4, 2001.
15. EP Petrov and DJ Ewins. Advanced modeling of underplatform friction dampers for analysis of bladed disk vibration. *Journal of Turbomachinery*, 129:143–150, 2007.
16. C. Firrone, S. Zucca, and M. Gola. Effect of static/dynamic coupling on the forced response of turbine bladed disks with underplatform dampers. volume 6, 2009.
17. L. Panning, K. Popp, W. Sextro, F. Götting, A. Kayser, and I. Wolter. Asymmetrical underplatform dampers in gas turbine bladings: Theory and application. volume 6, 2004.
18. G. Csaba. Modelling of a microslip friction damper subjected to translation and rotation. *Proceedings of the ASME Turbo Expo*, 1999.
19. M. Jareland. Experimental investigation of a platform damper with curved contact areas. volume 6 A, 2001.
20. S. Zucca, D. Botto, and M. Gola. Range of variability in the dynamics of semi-cylindrical friction dampers for turbine blades. volume 5, 2008.
21. M. Gola and C. Gastaldi. Understanding complexities in underplatform damper mechanics. volume 7A, 2014.
22. A. Bessone, F. Toso, and T. Berruti. Investigation on the dynamic response of blades with asymmetric under platform dampers. volume 7B, 2015.
23. E. Denimal, C. Wong, L. Salles, and L. Pesaresi. On the efficiency of a conical underplatform damper for turbines. *Journal of Engineering for Gas Turbines and Power*, 143, 2021.
24. *Optimization of the Contact Geometry Between Turbine Blades and Underplatform Dampers With Respect to Friction Damping*, volume Volume 4: Turbo Expo 2002, Parts A and B of *Turbo Expo: Power for Land, Sea, and Air*, 06 2002.
25. C. Gastaldi and M. Gola. Pre-optimization of asymmetrical underplatform dampers. *Journal of Engineering for Gas Turbines and Power*, 139, 2017.

26. W. Tang and B. Epureanu. Geometric optimization of dry friction ring dampers. *International Journal of Non-Linear Mechanics*, 109:40–49, 2019.
27. Y. Sun, J. Yuan, E. Denimal, and L. Salles. Nonlinear Modal Analysis of Frictional Ring Damper for Compressor Blisk. *Journal of Engineering for Gas Turbines and Power*, 143(3), 02 2021.
28. M. Krack, L. Panning-von Scheidt S. Tatzko, and J. Wallaschek. Reliability optimization of friction-damped systems using nonlinear modes. *Journal of Sound and Vibration*, 333(13):2699–2712, 2014.
29. Y. Yuan, A. Jones, R. Setchfield, and C.W. Schwingshackl. Robust design optimisation of underplatform dampers for turbine applications using a surrogate model. *Journal of Sound and Vibration*, 494:115528, 2021.
30. H. Eschenauer and N. Olhoff. Topology optimization of continuum structures: a review. *Appl. Mech. Rev.*, 54(4):331–390, 2001.
31. E. Raponi, M. Bujny, M. Olhofer, S. Boria, and F. Duddeck. Hybrid kriging-assisted level set method for structural topology optimization. In *IJCCI*, pages 70–81, 2019.
32. E. Raponi, M. Bujny, M. Olhofer, S. Boria, and F. Duddeck. Hybrid strategy coupling ego and cma-es for structural topology optimization in statics and crashworthiness. In *International Joint Conference on Computational Intelligence*, pages 55–84. Springer, 2019.
33. E. Raponi, M. Bujny, M. Olhofer, N. Aulig, S. Boria, and F. Duddeck. Kriging-assisted topology optimization of crash structures. *Computer Methods in Applied Mechanics and Engineering*, 348:730–752, 2019.
34. X. Guo, W. Zhang, and W. Zhong. Doing topology optimization explicitly and geometrically—a new moving morphable components based framework. *Journal of Applied Mechanics*, 81(8), 2014.
35. W. Zhang, J. Yuan, J. Zhang, and X. Guo. A new topology optimization approach based on moving morphable components (mmc) and the ersatz material model. *Structural and Multidisciplinary Optimization*, 53(6):1243–1260, 2016.
36. E. Denimal, F. El-haddad, C. Wong, and L. Salles. Topological optimization of under-platform dampers with moving morphable components and global optimization algorithm for nonlinear frequency response. *Journal of Engineering for Gas Turbines and Power*, 143(2), 2021.
37. M. Bujny, N. Aulig, M. Olhofer, and F. Duddeck. Learning-based topology variation in evolutionary level set topology optimization. In *Proceedings of the Genetic and Evolutionary Computation Conference*, pages 825–832, 2018.
38. M. Bendsøe and N. Kikuchi. Generating optimal topologies in structural design using a homogenization method. *Computer methods in applied mechanics and engineering*, 71(2):197–224, 1988.
39. M. Bendsøe. Optimal shape design as a material distribution problem. *Structural optimization*, 1(4):193–202, 1989.
40. Z-D Ma, N. Kikuchi, and I Hagiwara. Structural topology and shape optimization for a frequency response problem. *Computational mechanics*, 13(3):157–174, 1993.
41. M. Bendsøe and A. Díaz. Optimization of material properties for improved frequency response. *Structural optimization*, 7(1-2):138–140, 1994.
42. N. Pedersen. Maximization of eigenvalues using topology optimization. *Structural and multidisciplinary optimization*, 20(1):2–11, 2000.
43. S. Dou and J. Jensen. Optimization of nonlinear structural resonance using the incremental harmonic balance method. *Journal of Sound and Vibration*, 334:239–254, 2015.
44. S. Dou, B. Strachan, S. Shaw, and J. Jensen. Structural optimization for nonlinear dynamic response. *Philosophical Transactions of the Royal Society A: Mathematical, Physical and Engineering Sciences*, 373(2051):20140408, 2015.
45. Michael Yu Wang, Xiaoming Wang, and Dongming Guo. A level set method for structural topology optimization. *Computer methods in applied mechanics and engineering*, 192(1-2):227–246, 2003.
46. G. Allaire, F. Jouve, and A-M. Toader. A level-set method for shape optimization. *Comptes Rendus Mathematique*, 334(12):1125–1130, 2002.
47. J. Yuan, A. Fantetti, E. Denimal, S. Bhatnagar, L. Pesaresi, C. Schwingshackl, and L Salles. Propagation of friction parameter uncertainties in the nonlinear dynamic response of turbine blades with underplatform dampers. *Mechanical Systems and Signal Processing*, 156:107673, 2021.
48. W. Sextro. *Dynamical contact problems with friction*. Springer, 2007.
49. N. van Dijk, K. Maute, M. Langelaar, and F. Van Keulen. Level-set methods for structural topology optimization: a review. *Structural and Multidisciplinary Optimization*, 48(3):437–472, 2013.
50. V. Challis. A discrete level-set topology optimization code written in matlab. *Structural and multidisciplinary optimization*, 41(3):453–464, 2010.
51. Z. Li, T. Shi, and Q. Xia. Eliminate localized eigenmodes in level set based topology optimization for the maximization of the first eigenfrequency of vibration. *Advances in Engineering Software*, 107:59–70, 2017.
52. G. Von Groll and D. Ewins. The harmonic balance method with arc-length continuation in rotor/stator contact problems. *Journal of sound and vibration*, 241(2):223–233, 2001.
53. T. Detroux, L. Renson, L. Masset, and G. Kerschen. The harmonic balance method for bifurcation analysis of large-scale nonlinear mechanical systems. *Computer Methods in Applied Mechanics and Engineering*, 296:18–38, 2015.
54. R. Cameron and W. Martin. The orthogonal development of non-linear functionals in series of fourier-hermite functionals. *Annals of Mathematics*, pages 385–392, 1947.
55. L. Renson, T.L. Hill, D.A. Ehrhardt, D.A.W. Barton, and S.A. Neild. Force appropriation of nonlinear structures. *Proceedings of the Royal Society A: Mathematical, Physical and Engineering Sciences*, 474(2214):20170880, 2018.
56. D. Jones, M. Schonlau, and W. Welch. Efficient global optimization of expensive black-box functions. *Journal of Global optimization*, 13(4):455–492, 1998.

57. J. Kleijnen. Kriging metamodeling in simulation: A review. *European journal of operational research*, 192(3):707–716, 2009.
58. O. Roustant, D. Ginsbourger, and Y. Deville. Dicekriging, diceoptim: Two r packages for the analysis of computer experiments by kriging-based metamodeling and optimization. *Journal of statistical software*, 51(1):1–55, 2012.
59. D. Goldberg and J. Holland. Genetic algorithms and machine learning. *Machine Learning*, 3(2):95–99, 1988.

A Contact modelling

One contact element is represented in Figure 14 [12]. The normal contact force f_n at one point is given by:

$$f_n = \begin{cases} 0 & \text{for separation} \\ N_0 + k_n y & \text{for contact} \end{cases} \tag{24}$$

and the tangential contact force f_t by:

$$f_t = \begin{cases} 0 & \text{for separation} \\ f_t^0 + k_t(x - x_0) & \text{for stick} \\ -sign(\dot{x})\mu f_t & \text{for slip} \end{cases} \tag{25}$$

where μ is the friction coefficient, k_n is the normal contact stiffness, k_t is the tangential contact stiffness, N_0 is the normal pre-load, $x_0 = x(\tau_{stick})$ the displacement at the beginning of the stick-state and f_t^0 the tangential force at the beginning of the stick-state. A complete description of the contact formulation can be found in [12].

The initial contact pressure σ_0 at the contact interfaces is obtained from the equations of equilibrium of the centrifugal loading C_F, the friction forces and the normal forces applied to the UPD without accounting for the elastic deformation of the damper and blade platforms [15]. It is given by

$$\sigma_0 = \frac{1}{2}\frac{C_F}{A(\cos\alpha + \mu\sin\alpha)}, \tag{26}$$

where A is the contact area on each side of the damper and α is the damper angle (angle formed by the two contact surfaces). The centrifugal loading C_F is given by $C_F = m_{damper} \times R \times \omega_r^2$ where m_{damper} is the mass of the damper, R the radius, and ω the rotational speed. In the present case, for a full damper the mass m_{damper} is equal to 3.42 g, the radius is taken as the distance between the gravity center of the damper and the bottom of the base, and $\omega_r = 1402$ rad/s. In the case of a full damper, it gives $\sigma_0 = 9.8987$ N/mm. The normal contact stiffness k_n is set to 20000N/mm and the tangential contact stiffness k_t is assumed to be equal to k_n [48].

It is worth emphasizing here that the damper properties that are directly related to its geometry will be updated during the optimisation process, i.e. its mass, the radius and the contact area. This has a direct impact on the centrifugal loading and the normal pressure.

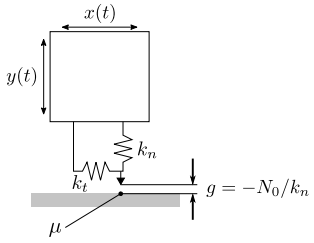

Fig. 14: 2D friction contact element